Research Article | Vol. 31, No. 6 / 13 Mar 2023 / Optics Express 10684

Optics EXPRESS

Compact nonvolatile polarization switch using an asymmetric Sb_2Se_3-loaded silicon waveguide

HUIMIN JIN,[1,2] LEI NIU,[1,2] JIAJIU ZHENG,[3] PEIPENG XU,[1,2,*] AND ARKA MAJUMDAR[3,4]

[1] *Faculty of Electrical Engineering and Computer Science, Ningbo University, Ningbo, 315211, China*
[2] *Key Laboratory of Photoelectric Detection Materials and Devices of Zhejiang Province, Ningbo, 315211, China*
[3] *Department of Electrical and Computer Engineering, University of Washington, Seattle, WA 98195, USA*
[4] *Department of Physics, University of Washington, Seattle, WA 98195, USA*
[*] *xupeipeng@nbu.edu.cn*

Abstract: We propose and simulate a compact (~29.5 μm-long) nonvolatile polarization switch based on an asymmetric Sb_2Se_3-clad silicon photonic waveguide. The polarization state is switched between TM_0 and TE_0 mode by modifying the phase of nonvolatile Sb_2Se_3 between amorphous and crystalline. When the Sb_2Se_3 is amorphous, two-mode interference happens in the polarization-rotation section resulting in efficient TE_0-TM_0 conversion. On the other hand, when the material is in the crystalline state, there is little polarization conversion because the interference between the two hybridized modes is significantly suppressed, and both TE_0 and TM_0 modes go through the device without any change. The designed polarization switch has a high polarization extinction ratio of > 20 dB and an ultra-low excess loss of < 0.22 dB in the wavelength range of 1520-1585 nm for both TE_0 and TM_0 modes.

1. Introduction

Silicon photonics has enabled low-cost, high-volume manufacturing of photonic integrated circuits (PIC) by realizing numerous optical functions on a chip utilizing the well-developed complementary metal-oxide-semiconductor (CMOS) fabrication technology [1,2]. The silicon photonic devices, however, are polarization-dependent due to the large index contrast between silicon and the top cladding (SiO_2 or air) of the waveguides [3]. To eliminate the issue, a polarization-diverse system consisting of the polarizing beam splitter (PBS) and polarization rotator (PR) is used to allow the components to work at a single polarization state [4]. The PR can provide essential functionalities in a diverse polarization circuit to convert polarization.

Different PRs can be grouped into two categories based on their working mechanism: mode-evolution and mode-hybridization-based PR. Mode-evolution-based PR typically adopts an adiabatic taper waveguide, which enables mode conversion with the gradual change of the waveguide structure [5,6]. In mode coupling, asymmetrical directional couplers are also broadly adopted because the phase-matching condition can be satisfied when the structural symmetry is broken [7,8]. Mode-hybridization-based PRs exploit special asymmetric structures to transfer optical power through the interference of the two hybridized modes [9–11].

However, most reported PRs are designed to produce only one polarization state, and once fabricated, their functionality cannot be changed. Reference [12] shows a polarization rotator with a polarization conversion efficiency of -0.51 dB over a bandwidth of 80 nm based on a symmetry-breaking silicon overlay. In Ref. [13], A. Tuniz *et al.* demonstrated a modular approach that consists of a plasmonic rotator and a focusing element to connect silicon-on-insulator waveguides to hybrid plasmonic integrated circuits. Reference [14] demonstrated a mode converter comprised of a silicon gradient metasurface on the $LiNbO_3$ waveguides. The transmission efficiency was 94.4%, averaged over 1480-1580 nm. In a PIC, reconfigurable polarization switches with the

#482817 https://doi.org/10.1364/OE.482817
Journal © 2023 Received 9 Dec 2022; revised 2 Feb 2023; accepted 21 Feb 2023; published 9 Mar 2023

Optics EXPRESS

ability to dynamically set versatile polarizations are highly desired. To date, only a very few polarization switches have been proposed. In Ref. [15], a polarization switch with a polarization extinction ratio of ~20 dB was demonstrated by cascading three PRs based on a dual trench waveguide and three electrically tunable phase shifters. In Ref. [16], Zhao *et al.* proposed and demonstrated a polarization switch using a 1×1 MZI. The excess losses were about 0.6 dB, and the polarization extinction ratios were > 20 dB for both TE and TM modes in the wavelength range of 1530-1600 nm. However, these polarization-switching implementations are volatile and power-hungry, and they suffer from large footprint of ~100-1000 μm). A compact and nonvolatile polarization switch that features low excess losses, high polarization extinction ratio, and broad bandwidths can be highly transformative.

Phase-change materials (PCMs) provide an attractive solution toward compact and energy-efficient reconfigurable photonic devices with zero static power [17–19], thanks to a nonvolatile phase transition and large refractive index contrast between two states. Chalcogenide PCMs such as $Ge_2Sb_2Te_5$ (GST) is the most commonly used PCMs, which have been employed in multifunctional devices such as photonic memories [20,21], optical switches [22–26], and optical neural networks [27,28]. However, GST-on-silicon hybrid waveguide suffers from high absorption loss in both crystalline and amorphous states [25], preventing its applicability to photonics. To further reduce the optical absorption of GST, $Ge_2Sb_2Se_4Te_1$ (GSST) was developed recently by substituting the atoms with Se atoms in GST. However, GSST still exhibits a high optical loss at 1550 nm in the crystalline state [29]. These limitations have motivated the development of wide bandgap PCMs such as Sb_2Se_3 and Sb_2S_3, demonstrating ultra-low-loss photonic devices [30–32]. In particular, Sb_2Se_3 exhibits no intrinsic absorption losses in both states and has a large refractive index contrast $\Delta n \approx 0.77$ [30].

In this work, we propose a compact polarization switch based on an asymmetric Sb_2Se_3-loaded waveguide connected with a regular silicon strip waveguide at the input and output ends. By carefully designing the structures, highly efficient polarization conversion can be realized using the interference between two hybridized modes supported in the polarization rotation section when the Sb_2Se_3 is in the amorphous state. In this case, the launched TE_0 (TM_0) mode completely converts to the fundament TM_0 (TE_0) mode with an appropriate conversion length. On the other hand, when the Sb_2Se_3 is switched to the crystalline state, the interference between two hybridized modes is suppressed. Consequently, the coupling between two waveguides is minimal, and one has a low-loss transmission for both polarizations.

2. Principle and design

Our device designs are largely motivated by experimental feasibility. Especially, we want to ensure that the PCM can be deposited via standard sputtering and lift-off techniques (hence, they are placed on top of the silicon waveguide) and the PCM can be switched reliably (hence, thin enough PCM is considered). Figure 1(a) shows the schematic of the proposed polarization switch, which consists of an asymmetric Sb_2Se_3-loaded waveguide connected with a regular silicon strip waveguide at the input and output ends. Figure 1(b) shows the cross section of the asymmetrical Sb_2Se_3-loaded waveguide, where a thin Sb_2Se_3 layer is placed at the corner of the silicon strip. In this way, the structure with cross-sectional asymmetry is introduced to hybridize the modes. For amorphous Sb_2Se_3, the parameters are chosen optimally to support two hybridized modes equally. As a result, when the TE_0 or TM_0 mode is launched from the input and enters the polarization-rotation section, two hybridized modes can be excited with equal mode-excitation ratios. Hence, the input TE_0 (TM_0) mode completely converts to TM_0 (TE_0) mode with an appropriate conversion length. On the other hand, for crystalline Sb_2Se_3, the interference between two hybridized modes is suppressed due to the highly unbalanced excited hybrid modes. We designed the device in the popular silicon-on-insulator (SOI) platform with silicon thickness $h_s = 340$ nm. The silicon and silica refractive indices are $n_{si} = 3.455$ and

Optics EXPRESS

n_{sio2} = 1.445, respectively, at 1550 nm. The upper cladding is chosen to be SiO_2 for protection or quasi-symmetry in the vertical direction. The refractive indices of amorphous Sb_2Se_3 (a-Sb_2Se_3) and crystalline Sb_2Se_3 (c-Sb_2Se_3) are taken as 3.3058 and 4.3281, respectively. There is no imaginary part of the index as measured via ellipsometry [33]. We note that the fundamental insight in designing these devices is to identify the interference conditions for full constructive or destructive interference. The mode-index from each waveguide can help calculate the interference condition. However, to find the exact condition of interference, we need to perform extensive electromagnetic simulations.

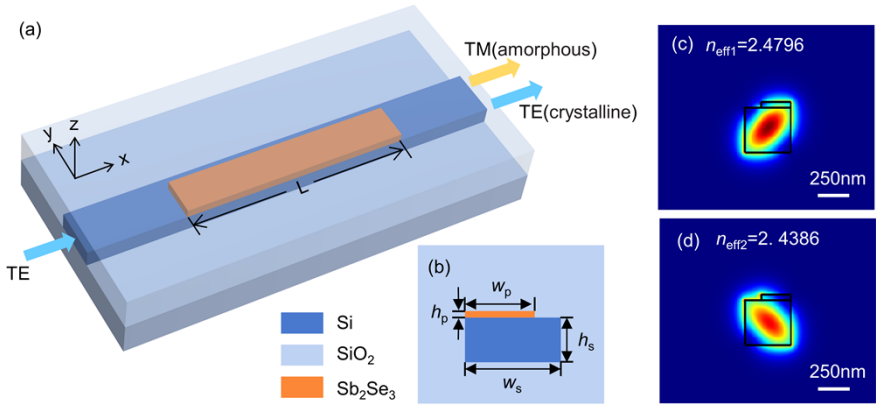

Fig. 1. (a) Schematic configuration of the proposed polarization switch. (b) The cross section of the polarization rotation region of the polarization switch. (c-d) Electric field profiles of the two lowest-order hybridized modes with a-Sb_2Se_3 at the wavelength of 1550 nm.

As mentioned above, the polarization rotation region is designed to equally excite two lowest-order hybridized modes when the Sb_2Se_3 is in the amorphous state. In this case, two-mode interference happens in the polarization-rotation section with a beat length given by $L = L_c = \pi/(\beta_0 - \beta_1)$, where β_0 and β_1 are, respectively, the propagation constants of two hybridized modes. Figures 1(c) and 1(d) show the calculated electric field profiles where strong polarization hybridization can be observed. Here, we use the polarization conversion efficiency (PCE, defined as the ratio of the desired polarization to the sum of both polarizations at the output port) to analyze the performance of polarization conversion, which can be expressed as follows [9]:

$$\mathrm{PCE} = \sin^2(2\theta)\sin^2\left(\frac{\pi L}{2L_c}\right) \times 100\% \tag{1}$$

Here, θ denotes the polarization rotation angle of the two lowest-order eigenmodes, defined as [34,35]:

$$\tan(\theta) = R = \frac{\iint_{\Omega} n^2(x,y) \cdot H_x^2(x,y)dxdy}{\iint_{\Omega} n^2(x,y) \cdot H_y^2(x,y)dxdy} \tag{2}$$

where R is the polarization rotation parameter, $n(x,y)$ is the refractive-index distribution, and the magnetic-field components $H_x(x,y)$ and $H_y(x,y)$ are the transverse and horizontal components of the specified eigenmode, respectively. The optical axis rotation angle $\theta = 45^\circ$ is required to realize a 100% polarization conversion with a conversion length of $L = L_c$.

The polarization rotation angle θ is closely associated with the width (w_p) and height (h_p) of the Sb_2Se_3. To determine the structure parameters appropriately, we analyze the field distribution

Optics EXPRESS

of the hybrid modes supported in the asymmetric waveguide. Figure 2 shows the optical axis rotation angle θ as a function of w_p and h_p with different strip widths (w_s) when it is in a-Sb_2Se_3 and c-Sb_2Se_3 state at 1550 nm. Since we aim to achieve polarization conversion in the Sb_2Se_3 amorphous state, we need to choose the appropriate parameters along the contour line with $\theta = 45°$ as shown in Figs. 2(a)-(c). We find a range of w_p and h_p that can achieve 100% conversion efficiency (corresponding to different conversion lengths) in the amorphous state. We note that, to ensure reliable phase transition with high endurance, the PCM layer should be thin and of lower volume. From the figure, one can find that a small strip width w_s with lower volume (as well as smaller w_p and h_p) is preferred to achieve modulation of the optical axis rotation angle. To achieve highly unbalanced excited hybrid modes in the crystalline state, it is essential to deviate the rotation angle θ away from 45° (as shown in Figs. 2(d)-(f)). However, due to the asymmetry of the structure with c-Sb_2Se_3, the input polarized light will still be partially transformed into the orthogonal mode. Two different beat lengths will be generated corresponding to the two states of Sb_2Se_3. Here, the beat lengths of a-Sb_2Se_3 and c-Sb_2Se_3 states are represented by L_{c-a} and $L_{c-c,}$ respectively. The L_{c-c} can be carefully designed to be half of L_{c-a}, allowing the transfer of optical power to orthogonal mode and back again.

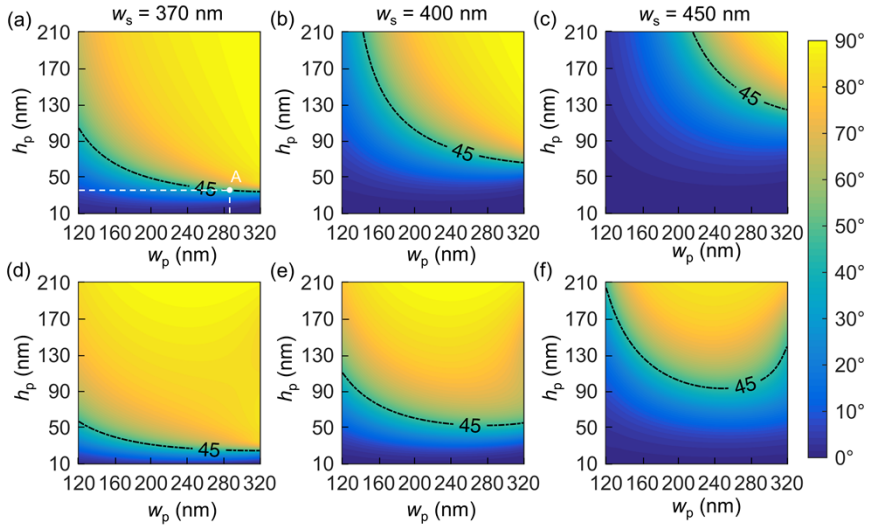

Fig. 2. The calculated polarization rotation angle θ with varied w_p and h_p with different strip width w_s in the Sb_2Se_3 (a)-(c) amorphous and (d)-(f) crystalline state, respectively.

Figure 3(a) shows the calculated transition loss due to the mode mismatch at the junction as a function of w_s in the a-Sb_2Se_3 state, including input (TL-in) and output (TL-out) transition loss. The transition losses are calculated from the overlap integral between the input/output waveguide at the ends and the asymmetric Sb_2Se_3-loaded waveguide at the polarization rotation section. We used the finite difference eigenmode (FDE) method (Lumerical MODE Solution) to perform the mode analysis. It is noted that the TL-out increases as the silicon strip width w_s increases, while the TL-in remains as low as ~0.05 dB. Hence, we choose w_s = 370 nm to minimize intrinsic loss and ensure single-mode operation. Figure 3(b) shows the total transition w_p loss in the a-Sb_2Se_3 state and beat length ratio (L_{c-a}/L_{c-c}) for different (h_p is chosen optimally to ensure the $\theta = 45°$). he transition losses are below 0.08 dB as the width w_p increases. To ensure that the polarization switch has high performance in both a-Sb_2Se_3 and c-Sb_2Se_3 states, we choose w_p = 285 nm and h_p = 35 nm (point A in Fig. 2(a)), in which a relatively low TL can be obtained while the beat length ratio is ~2. The corresponding conversion length is calculated as compact as L_{c-a} = ~29.5 μm.

Optics EXPRESS

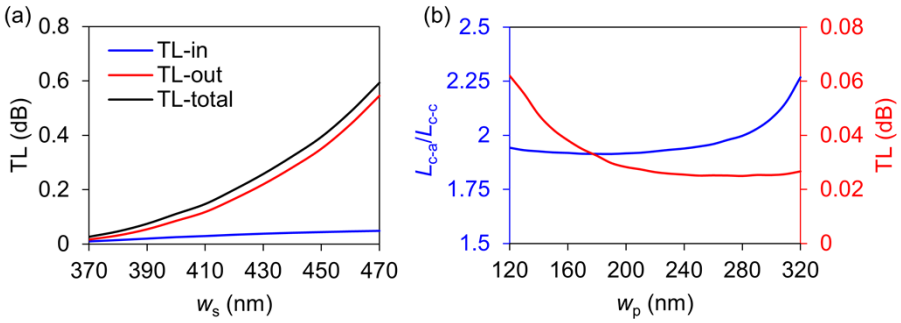

Fig. 3. (a) Calculated transition losses as a function of silicon strip width w_s in the a-Sb_2Se_3 state. (b) Calculated beat length ratios L_{c-a}/L_{c-c} and total transition loss in the a-Sb_2Se_3 state as the w_p varies. All the simulations are based on the optimal geometry parameters to ensure the $\theta = 45°$ in the a-Sb_2Se_3 state.

3. Simulation and performance

To verify the expected performance of the proposed polarization switch, we simulate the structure using a 3D finite-difference-time-domain method (Lumerical FDTD Solution). We restrict the simulation workplace of 34 μm × 3 μm × 4 μm in the three dimensions with perfectly matched layers (PML) used as boundaries. Our simulation employs mesh grid sizes of $\Delta x = \Delta y = 20$ nm and $\Delta z = 22$ nm. To denote the thickness of Sb_2Se_3 and ensure an accurate field distribution, we use a mesh grid size of $\Delta z = 5$ nm to override the Sb_2Se_3 domain. Figure 4 depicts the evolution of E_y and E_z components along the light propagation direction when the TE_0 mode (E_y component dominant) is launched into the input port in the a-Sb_2Se_3 and c-Sb_2Se_3 states, respectively. From Figs. 4(a) and 4(b), the E_y component gradually vanishes in the rotation section. In contrast, the E_z component begins to appear and becomes dominant in the output section when it is in the a-Sb_2Se_3 state. At the end of the polarization-rotation section, almost all the power is transferred to the orthogonally TM_0 mode in the a-Sb_2Se_3 state. The residual TE_0 power is negligible, indicating efficient conversion from input TE_0 to output TM_0 mode. On the other hand, the E_y component first weakens and strengthens when switched to the c-Sb_2Se_3 state, as shown in Figs. 4(c)–4(d). The initial weakening happens even in the c-Sb_2Se_3 state. There are two excited and differently weighted hybrid modes (the balance of two hybrid modes in the polarization conversion part is broken since the rotation angle θ deviates from 45°). There is little polarization conversion since only a small amount of field interference between the hybrid modes occurs. This can be verified from Figs. 4(c)–4(d), which show that TE_0 mode is first partially converted to TM_0 mode and then back to TE_0 mode. Figure 4(e) shows the mode profile distribution at different locations. One can find that there is an evolutionary process, i.e., in the a-Sb_2Se_3 state, the input TE_0 mode is converted to hybridized mode at the polarization-rotation section and then output as TM_0 mode. In contrast, the output light remains TE-polarized despite a small amount of interference between the two hybridized modes in the c-Sb_2Se_3 state.

Figure 5 shows the calculated polarization extinction ratio (PER) and excess loss (EL) spectra to assess the performance of the polarization switch. Here, the PER and EL in the a-Sb_2Se_3 state are defined as [36]:

$$PER = 10\log_{10}(T_{TE-TM}/T_{TE-TE}) \tag{3}$$

$$EL = -10\log_{10}(T_{TE-TM}) \tag{4}$$

Similarly, when it is switched to the c-Sb_2Se_3 state, the corresponding PER and EL are defined as:

$$PER = 10\log_{10}(T_{TE-TE}/T_{TE-TM}) \tag{5}$$

Optics EXPRESS

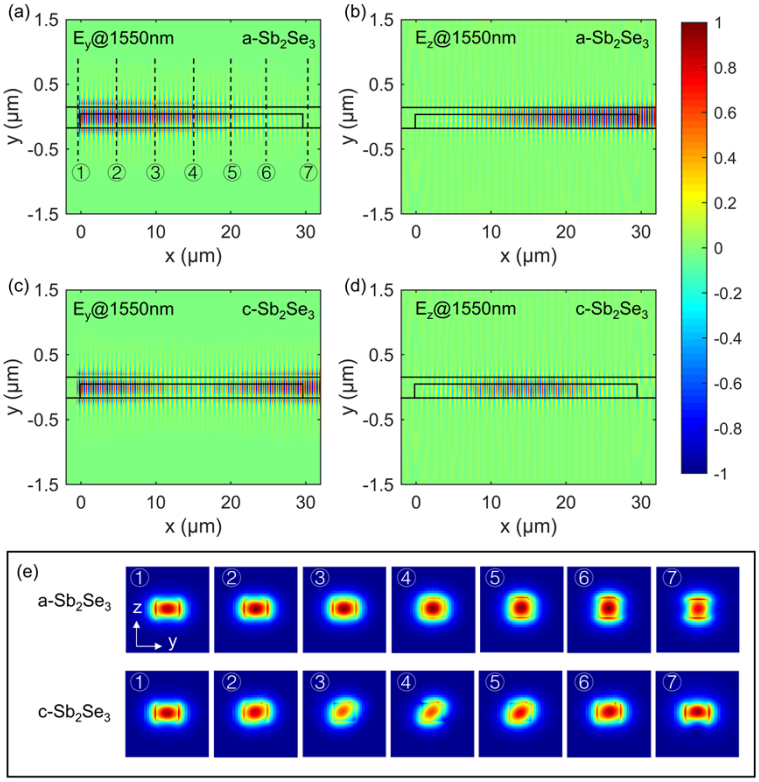

Fig. 4. Normalized electric field (a) E_y and (b) E_z propagation profiles of the designed polarization switch with Sb_2Se_3 in the amorphous state; Normalized electric field (c) E_y and (d) E_z propagation profiles of the designed polarization switch with Sb_2Se_3 in the crystalline state. (e) Field intensity profile of the device at the corresponding positions in (a). All the profiles are simulated when TE_0 mode is launched at the input end at 1550 nm.

$$EL = -10\log_{10}(T_{TE-TE}) \tag{6}$$

where T_{TE-TM} and T_{TE-TE} are the TM and TE transmittance for the launched TE_0 mode.

Figures 5(a)–5(b) show the calculated spectral responses of the designed polarization switch with Sb_2Se_3 in the amorphous and crystalline states when TE_0 mode is launched. When operating in the a-Sb_2Se_3 state, a PER > 20 dB and EL < 0.07 dB can be achieved across the 1520-1585 nm wavelength, while PER (EL) reaches 39.7 dB (0.04 dB) at central wavelength, as shown in Fig. 5(a). When it is switched to the c-Sb_2Se_3 state, almost no polarization rotation is observed, and the input TE_0 mode has an EL of < 0.22 dB and a high PER of > 20 dB in the wavelength range of 1520-1585 nm without polarization conversion. Furthermore, the transmission performance of the polarization switch for the launched TM_0 mode is also analyzed. The simulations show that the PERs are > 20 dB in both the a-Sb_2Se_3 and c-Sb_2Se_3 states over a broad wavelength band from 1520 nm to 1585 nm. Besides, the designed polarization switch shows low EL < 0.03 dB in the a-Sb_2Se_3 state and EL < 0.13 dB in the c-Sb_2Se_3 state, respectively. Sb_2Se_3 is an ultra-low loss PCM that exhibits negligible intrinsic absorption losses ($\kappa < 10^{-5}$) in both states [26,33]. However, recent research characterized waveguides with long Sb_2Se_3 (25 nm thick and 500 nm wide) patch lengths of 200-800 μm [30]. The results show that in the amorphous phase, the loss of any length is within the error range of insertion loss (±0.9 dB), even for patches approaching a millimeter in length. In the crystalline phase, the propagation loss was measured as 0.01 dB

Optics EXPRESS

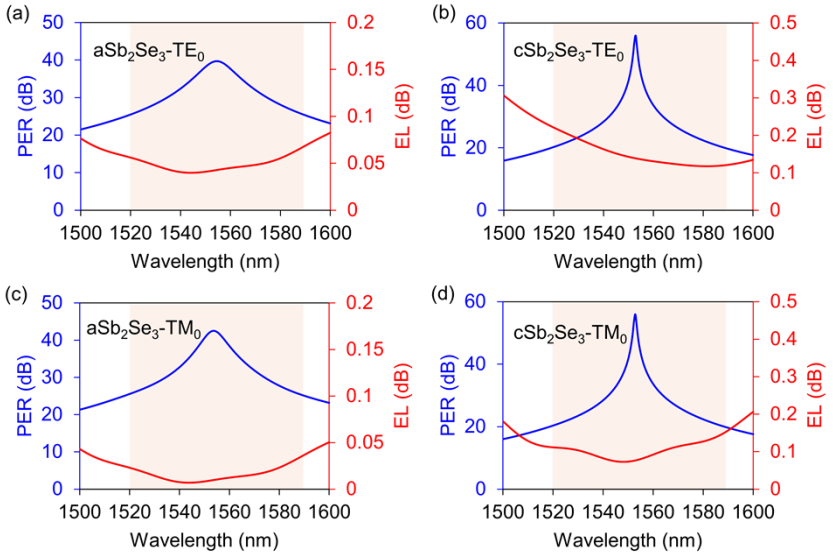

Fig. 5. Wavelength dependence of the PER and EL for the proposed polarization switch with a-Sb_2Se_3 (a) and c-Sb_2Se_3 (b) for the launched TE_0 modes; wavelength dependency of the PER and EL for the proposed polarization switch with a-Sb_2Se_3 (c) and c-Sb_2Se_3 (d) for the launched TM_0 modes. The orange-shaded areas represent the wavelength range of PER > 20 dB.

μm^{-1}. Based on this, we can deduce the imaginary part κ of the c-Sb_2Se_3 to be 0.0049. We then simulated the transmission spectra of the designed polarization switch, taking into account the absorption loss of the c-Sb_2Se_3. When the TE_0 (TM_0) mode is launched from the input end, the corresponding EL of our polarization switch would be less than 0.52 dB (0.51 dB) over the entire band for a 29.5 µm long Sb_2Se_3 patch in the crystalline state. This is still acceptable for practical use. Overall, the performance of the proposed polarization switch is essentially the same for the launched TE_0 and TM_0 modes.

4. Fabrication and tolerance

The proposed polarization switch based on the asymmetrical structure requires two-step E-beam lithography processes, including one silicon strip fabrication process and the Sb_2Se_3 lift-off process. When manufacturing errors occur, the modal field distribution will deviate from the designed values in both a-Sb_2Se_3 and c-Sb_2Se_3 states. Consequently, the optical axis rotation angle is no longer 45°, and the optimal polarization conversion length changes. To verify the robustness of the designed polarization switch, we analyze the fabrication tolerances on the alignment accuracy δx and the deviated width Δw_p of Sb_2Se_3. Figures 6(a) and 6(b) show the PER and EL of the device as a function of alignment accuracy δx (the distance between the Sb_2Se_3 layer and the edge of the silicon strip as shown in the inset) when TE_0 mode is launched. When it is in an amorphous Sb_2Se_3 state, the device attains an EL < 0.19 dB and PER > 14 dB with $\delta x = 5$ nm, as shown in Fig. 6(a), while the EL < 0.4 dB and PER > 12 dB can be achieved in the crystalline state which is shown in Fig. 6(b). Figures 6(c) and 6(d) show the PER and EL as a function of fabrication errors Δw_p. The PER is > 12 dB in both Sb_2Se_3 states with $\Delta w_p = \pm 10$ nm, while the EL is < 0.2 dB for the a-Sb_2Se_3 state and < 0.38 dB for the c-Sb_2Se_3 state, which is still acceptable. The properties of the polarization switch are more sensitive with alignment accuracy, posing a challenge to fabrication. But a more efficient heating method, such as using a monolayer graphene heater which allows for thick Sb_2Se_3 [26], may improve the fabrication tolerances.

Optics EXPRESS

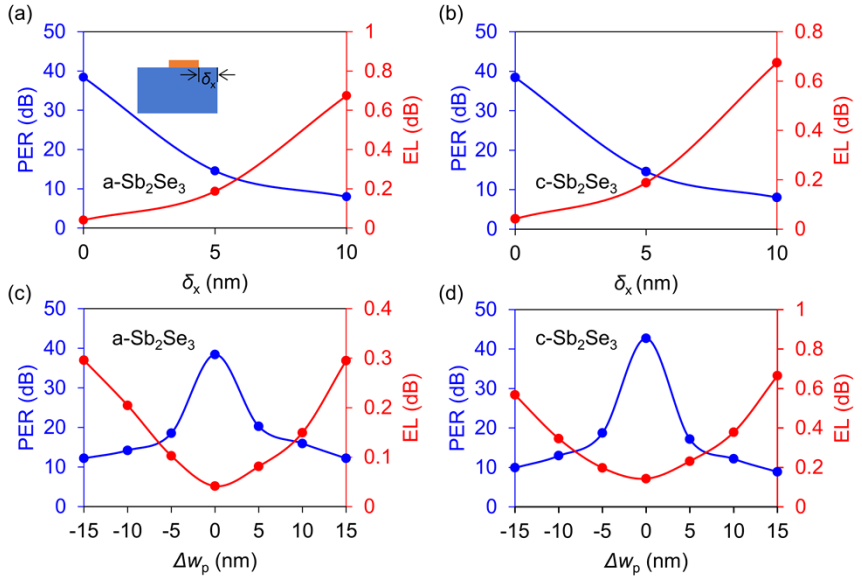

Fig. 6. PER and EL of the designed polarization switch at the wavelength of 1550 nm with the deviation of (a-b) δ_x and(c-d) Δw_p when in the amorphous and crystalline state, respectively. The smooth lines are guides to the eye to understand the trend.

5. Conclusion

We have proposed and designed a high-performance polarization switch based on an asymmetric Sb_2Se_3-loaded waveguide. The polarization states of light can be switched by tuning the state of the low-loss phase change material Sb_2Se_3. Two-mode interference occurs in the polarization-rotation section for the amorphous state, resulting in a complete TE_0-TM_0 conversion with the appropriate conversion length. However, there is negligible polarization conversion when it transitions to the crystalline state because the interference between the two hybridized modes is depressed. Consequently, one has a low-loss transmission for both polarizations. A 3D-FDTD simulation has been given for the optimal design of the polarization switch. The ELs are < 0.22 dB, and the PERs are > 20 dB for both polarization modes in the 1520-1585 nm wavelength range. Furthermore, the present polarization switch has a compact footprint of 29.5 μm × 0.37 μm. We also prove that the device possesses a relatively large fabrication tolerance. Our proposed concept of a nonvolatile polarization switch, especially its realization on a chip, will find numerous applications for more flexible signal processing, information sensing, and photonic interconnect.

Funding. National Key Research and Development Program of China (2021YFB2801300); Natural Science Foundation of Zhejiang Province (LD22F040002); National Natural Science Foundation of China (61875099); Natural Science Foundation of Ningbo (202003N4007); 3315 Innovation Team in Ningbo City; K. C. Wong Magna Fund in Ningbo University.

Disclosures. The authors declare no conflicts of interest.

Data availability. Data underlying the results presented in this paper are not publicly available at this time but may be obtained from the authors upon reasonable request.

References

1. L. Chrostowski and M. Hochberg, *Silicon photonics design: from devices to systems* (Cambridge University Press, 2015).
2. W. Bogaerts and L. Chrostowski, "Silicon Photonics Circuit Design: Methods, Tools and Challenges," Laser Photonics Rev. **12**(4), 1700237 (2018).

Optics EXPRESS

3. D. Dai, "Advanced Passive Silicon Photonic Devices With Asymmetric Waveguide Structures," Proc. IEEE **106**(12), 2117–2143 (2018).
4. T. Barwicz, M. R. Watts, M. A. Popović, P. T. Rakich, L. Socci, F. X. Kärtner, E. P. Ippen, and H. I. Smith, "Polarization-transparent microphotonic devices in the strong confinement limit," Nat. Photonics **1**(1), 57–60 (2007).
5. K. Goi, A. Oka, H. Kusaka, K. Ogawa, T.-Y. Liow, X. Tu, G.-Q. Lo, and D.-L. Kwong, "Low-loss partial rib polarization rotator consisting only of silicon core and silica cladding," Opt. Lett. **40**(7), 1410–1413 (2015).
6. L. Chen, C. R. Doerr, and Y.-K. Chen, "Compact polarization rotator on silicon for polarization-diversified circuits," Opt. Lett. **36**(4), 469–471 (2011).
7. L. Liu, Y. Ding, K. Yvind, and J. M. Hvam, "Silicon-on-insulator polarization splitting and rotating device for polarization diversity circuits," Opt. Express **19**(13), 12646–12651 (2011).
8. Y. Ding, L. Liu, C. Peucheret, and H. Ou, "Fabrication tolerant polarization splitter and rotator based on a tapered directional coupler," Opt. Express **20**(18), 20021–20027 (2012).
9. Z. Wang and D. Dai, "Ultrasmall Si-nanowire-based polarization rotator," J. Opt. Soc. Am. B **25**(5), 747–753 (2008).
10. M. Aamer, A. M. Gutierrez, A. Brimont, D. Vermeulen, G. Roelkens, J. M. Fedeli, A. Hakansson, and P. Sanchis, "CMOS Compatible Silicon-on-Insulator Polarization Rotator Based on Symmetry Breaking of the Waveguide Cross Section," IEEE Photon. Technol. Lett. **24**(22), 2031–2034 (2012).
11. A. V. Velasco, M. L. Calvo, P. Cheben, A. Ortega-Moñux, J. H. Schmid, C. A. Ramos, ÍM Fernandez, J. Lapointe, M. Vachon, S. Janz, and D.-X. Xu, "Ultracompact polarization converter with a dual subwavelength trench built in a silicon-on-insulator waveguide," Opt. Lett. **37**(3), 365–367 (2012).
12. D. Vermeulen, S. Selvaraja, P. Verheyen, P. Absil, W. Bogaerts, D. V. Thourhout, and G. Roelkens, "Silicon-on-Insulator Polarization Rotator Based on a Symmetry Breaking Silicon Overlay," IEEE Photon. Technol. Lett. **24**(6), 482–484 (2012).
13. A. Tuniz, O. Bickerton, F. J. Diaz, T. Käsebier, E.-B. Kley, S. Kroker, S. Palomba, and C. M. de Sterke, "Modular nonlinear hybrid plasmonic circuit," Nat. Commun. **11**(1), 2413 (2020).
14. Z. Li, M.-H. Kim, C. Wang, Z. Han, S. Shrestha, A. C. Overvig, M. Lu, A. Stein, A. M. Agarwal, M. Lončar, and N. Yu, "Controlling propagation and coupling of waveguide modes using phase-gradient metasurfaces," Nat. Nanotechnol. **12**(7), 675–683 (2017).
15. J. D. Sarmiento-Merenguel, R. Halir, X. Le Roux, C. Alonso-Ramos, L. Vivien, P. Cheben, E. Durán-Valdeiglesias, I. Molina-Fernández, D. Marris-Morini, D. X. Xu, J. H. Schmid, S. Janz, and A. Ortega-Moñux, "Demonstration of integrated polarization control with a 40 dB range in extinction ratio," Optica **2**(12), 1019–1023 (2015).
16. W. Zhao, R. Liu, Y. Peng, X. Yi, H. Chen, and D. Dai, "High-performance silicon polarization switch based on a Mach–Zehnder interferometer integrated with polarization-dependent mode converters," Nanophotonics **11**(10), 2293–2301 (2022).
17. M. Wuttig, H. Bhaskaran, and T. Taubner, "Phase-change materials for nonvolatile photonic applications," Nat. Photonics **11**(8), 465–476 (2017).
18. Z. Fang, R. Chen, J. Zheng, and A. Majumdar, "Nonvolatile Reconfigurable Silicon Photonics Based on Phase-Change Materials," IEEE J. Sel. Top. Quantum Electron. **28**(3), 8200317 (2021).
19. S. Abdollahramezani, O. Hemmatyar, H. Taghinejad, A. Krasnok, Y. Kiarashinejad, M. Zandehshahvar, A. Alù, and A. Adibi, "Tunable nanophotonics enabled by chalcogenide phase-change materials," Nanophotonics **9**(5), 1189–1241 (2020).
20. C. Ríos, M. Stegmaier, P. Hosseini, D. Wang, T. Scherer, C. D. Wright, H. Bhaskaran, and W. H. P. Pernice, "Integrated all-photonic nonvolatile multi-level memory," Nat. Photonics **9**(11), 725–732 (2015).
21. X. Li, N. Youngblood, C. Ríos, Z. Cheng, C. D. Wright, W. H. P. Pernice, and H. Bhaskaran, "Fast and reliable storage using a 5 bit, nonvolatile photonic memory cell," Optica **6**(1), 1–6 (2019).
22. C. Wu, H. Yu, H. Li, X. Zhang, I. Takeuchi, and M. Li, "Low-Loss Integrated Photonic Switch Using Subwavelength Patterned Phase Change Material," ACS Photonics **6**(1), 87–92 (2019).
23. P. Xu, J. Zheng, J. K. Doylend, and A. Majumdar, "Low-Loss and Broadband Nonvolatile Phase-Change Directional Coupler Switches," ACS Photonics **6**(2), 553–557 (2019).
24. R. Chen, Z. Fang, J. E. Fröch, P. Xu, J. Zheng, and A. Majumdar, "Broadband Nonvolatile Electrically Controlled Programmable Units in Silicon Photonics," ACS Photonics **9**(6), 2142–2150 (2022).
25. J. Zheng, Z. Fang, C. Wu, S. Zhu, P. Xu, J. K. Doylend, S. Deshmukh, E. Pop, S. Dunham, M. Li, and A. Majumdar, "Nonvolatile Electrically Reconfigurable Integrated Photonic Switch Enabled by a Silicon PIN Diode Heater," Adv. Mater. **32**(31), 2001218 (2020).
26. Z. Fang, R. Chen, J. Zheng, A. I. Khan, K. M. Neilson, S. J. Geiger, D. M. Callahan, M. G. Moebius, A. Saxena, M. E. Chen, C. Rios, J. Hu, E. Pop, and A. Majumdar, "Ultra-low-energy programmable nonvolatile silicon photonics based on phase-change materials with graphene heaters," Nat. Nanotechnol. **17**(8), 842–848 (2022).
27. J. Feldmann, N. Youngblood, C. D. Wright, H. Bhaskaran, and W. H. P. Pernice, "All-optical spiking neurosynaptic networks with self-learning capabilities," Nature **569**(7755), 208–214 (2019).
28. J. Feldmann, N. Youngblood, M. Karpov, H. Gehring, X. Li, M. Stappers, M. Le Gallo, X. Fu, A. Lukashchuk, A. S. Raja, J. Liu, C. D. Wright, A. Sebastian, T. J. Kippenberg, W. H. P. Pernice, and H. Bhaskaran, "Parallel convolutional processing using an integrated photonic tensor core," Nature **589**(7840), 52–58 (2021).
29. Y. Zhang, J. B. Chou, and J. Li, *et al.*, "Broadband transparent optical phase change materials for high-performance nonvolatile photonics," Nat. Commun. **10**(1), 4279 (2019).

Optics EXPRESS

30. M. Delaney, I. Zeimpekis, D. Lawson, D. W. Hewak, and O. L. Muskens, "A New Family of Ultralow Loss Reversible Phase-Change Materials for Photonic Integrated Circuits: Sb^2S_3 and Sb_2Se_3," Adv. Funct. Mater. **30**(36), 2002447 (2020).
31. Z. Fang, J. Zheng, A. Saxena, J. Whitehead, Y. Chen, and A. Majumdar, "Nonvolatile Reconfigurable Integrated Photonics Enabled by Broadband Low-Loss Phase Change Material," Adv. Optical Mater. **9**(9), 2002049 (2021).
32. M. Delaney, I. Zeimpekis, H. Du, X. Yan, M. Banakar, D. J. Thomson, D. W. Hewak, and O. L. Muskens, "Nonvolatile programmable silicon photonics using an ultralow-loss Sb_2Se_3 phase change material," Sci. Adv. **7**(25), eabg3500 (2021).
33. Z. Fang, R. Chen, J. Zhang, P. Xu, and A. Majumdar, "Low-loss broadband nonvolatile 2×2 switch based on Sb_2Se_3 for programmable silicon photonics," in *Conference on Lasers and Electro-Optics, Technical Digest Series* (Optica Publishing Group, 2022), STh4G.6.
34. H. Deng, D. O. Yevick, C. Brooks, and P. E. Jessop, "Design Rules for Slanted-Angle Polarization Rotators," J. Lightwave Technol. **23**(1), 432–445 (2005).
35. V. P. Tzolov and M. Fontaine, "A passive polarization converter free of longitudinally-periodic structure," Opt. Commun. **127**(1-3), 7–13 (1996).
36. H. Xu and Y. Shi, "Subwavelength-grating-assisted silicon polarization rotator covering all optical communication bands," Opt. Express **27**(4), 5588–5597 (2019).